

Ferroelectric Domain Control of Nonlinear Light Polarization in MoS₂ via PbZr_{0.2}Ti_{0.8}O₃ Thin Films and Free-Standing Membranes

Dawei Li, Xi Huang, Qiuchen Wu, Le Zhang, Yongfeng Lu, and Xia Hong*

Two-dimensional (2D) transition metal dichalcogenides (TMDCs) such as MoS₂ exhibit exceptionally strong nonlinear optical responses, while nanoscale control of the amplitude, polar orientation, and phase of the nonlinear light in TMDCs remains challenging. In this work, by interfacing monolayer MoS₂ with epitaxial PbZr_{0.2}Ti_{0.8}O₃ (PZT) thin films and free-standing PZT membranes, the amplitude and polarization of the second harmonic generation (SHG) signal are modulated via ferroelectric domain patterning, which demonstrates that PZT membranes can lead to in-operando programming of nonlinear light polarization. The interfacial coupling of the MoS₂ polar axis with either the out-of-plane polar domains of PZT or the in-plane polarization of domain walls tailors the SHG light polarization into different patterns with distinct symmetries, which are modeled via nonlinear electromagnetic theory. This study provides a new material platform that enables reconfigurable design of light polarization at the nanoscale, paving the path for developing novel optical information processing, smart light modulators, and integrated photonic circuits.

mixing.^[1–6] These functionalities make them a versatile playground for exploring ultrafast light-matter interaction and developing nanophotonic and optoelectronic applications, ranging from wavelength conversion,^[7,8] attosecond pulse generation,^[6,9] optical parametric generation,^[10] nonlinear valley optics,^[11–13] and quantum photonics.^[14,15] In previous studies, the optical nonlinearity in TMDCs has been tuned via strain,^[16–18] electrical field,^[7,19] artificial stacking,^[20–22] and plasmonic nanostructures.^[10,21,23] However, most of the efforts have been limited to the amplitude modulation. The polarization and geometric phase control have only been realized by integrating ultrathin TMDCs with plasmonic nano-sieves.^[24] The ability to modulate the amplitude, polar orientation, and phase of nonlinear light at the nanoscale is of enormous research interest for designing novel photonic

materials and developing quantum information applications, while in-operando programming is challenging and remains to be demonstrated.

A promising approach to tune the nonlinear optical response in 2D TMDC is to interface it with ferroelectrics.^[25,26] The nonvolatile, reconfigurable ferroelectric polarization has previously been exploited to introduce various novel functionalities into TMDCs, including nonvolatile memory,^[27,28] programmable homo- and hetero-junctions,^[29–31] directional transport mapping,^[32,33] voltage-controlled structural phase transition,^[34] photoluminescence and exciton modulation,^[35–37] and nonlinear optical filtering.^[38] The distinct polar orientation of ferroelectric domains and domain walls (DWs) can be further utilized to tailor the polar symmetry at ferroelectric/TMDC hetero-interfaces.^[38] Unlike the electric field effect approach,^[7] which is only effective for excitations at the excitonic resonance in the low-temperature environment, the interface polar coupling enabled tuning effect does not require the resonant or above-gap excitation condition and thus is viable for a wide range of temperature and light wavelength.

In this work, we exploit ferroelectric domain patterning to achieve nanoscale control of the magnitude and polarization of SHG in monolayer (1L) MoS₂ interfaced with epitaxial PbZr_{0.2}Ti_{0.8}O₃ (PZT) thin films and free-standing membranes in different stacking geometries. The SHG light polarization exhibits threefold symmetry (C_{3v}) at the polar domain regions

1. Introduction


Two-dimensional (2D) transition metal dichalcogenides (TMDCs) exhibit exceptionally strong nonlinear optical responses, including the second harmonic generation (SHG), third and higher order harmonic generation, and four wave

D. Li, Q. Wu, L. Zhang, X. Hong
Department of Physics and Astronomy
University of Nebraska-Lincoln
Lincoln, Nebraska 68588-0299, USA
E-mail: xia.hong@unl.edu

D. Li
School of Optoelectronic Engineering and Instrumentation Science
Dalian University of Technology
Dalian, Liaoning 116024, China

X. Huang, Y. Lu
Department of Electrical and Computer Engineering
University of Nebraska-Lincoln
Lincoln, Nebraska 68588-0511, USA

Y. Lu, X. Hong
Nebraska Center for Materials and Nanoscience
University of Nebraska-Lincoln
Lincoln, Nebraska 68588-0298, USA

 The ORCID identification number(s) for the author(s) of this article can be found under <https://doi.org/10.1002/adma.202208825>.

DOI: 10.1002/adma.202208825

and twofold symmetry (C_{2v}) at the ferroelectric DWs, which can be attributed to the interfacial coupling of the MoS_2 polar axis with either the out-of-plane spontaneous polarization of PZT or the chiral dipole rotation induced in-plane polarization at the DW, respectively, as modeled by nonlinear electromagnetic theory. Stacking a free-standing PZT membrane on top of MoS_2 can potentially lead to in-operando programming of light polarization, opening up new opportunities for developing smart nano-photonics, optical information processing, and photon-based quantum computing.

2. Results and Discussion

We mechanically exfoliate MoS_2 flakes on gel-films and identify 1L and bilayer (2L) flakes using Raman and photoluminescence (PL) spectra (Figure S1, Supporting Information). The crystalline orientation of MoS_2 is determined by polarization resolved SHG measurements. Selected flakes are interfaced with 50 nm

(001) PZT films in two different stacking sequences. The fabrication details of PZT samples can be found in the Experimental Section. In the first stacking geometry (denoted as MoS_2/PZT), we prepattern polarization up (P_{up}) and down (P_{dn}) domains on epitaxial PZT films deposited on 10 nm $\text{La}_{0.67}\text{Sr}_{0.33}\text{MnO}_3$ (LSMO) buffered SrTiO_3 (STO) substrates and transfer the MoS_2 flakes on top (Figure 1a). In the second structure (denoted as PZT/MoS_2), we transfer MoS_2 flakes on LSMO/STO and stack free-standing (001) PZT/LSMO membranes on top, followed by domain writing (Figure 1b). For both sample geometries, the zig-zag direction (a -axis) of MoS_2 is aligned with the horizontal DWs ([100] PZT). The domain structures are imaged using piezoresponse force microscopy (PFM) and SHG mapping (Experimental Section). Figure 1c shows the experimental setup for SHG imaging, where the incident laser beam (wavelength: 800 nm) propagates along \hat{z} direction (or $[00\bar{1}]$ orientation of PZT). The SHG signal is collected in both transmission (T-SHG) and reflection (R-SHG) modes. The polar SHG measurements are performed by rotating the incident light polarization

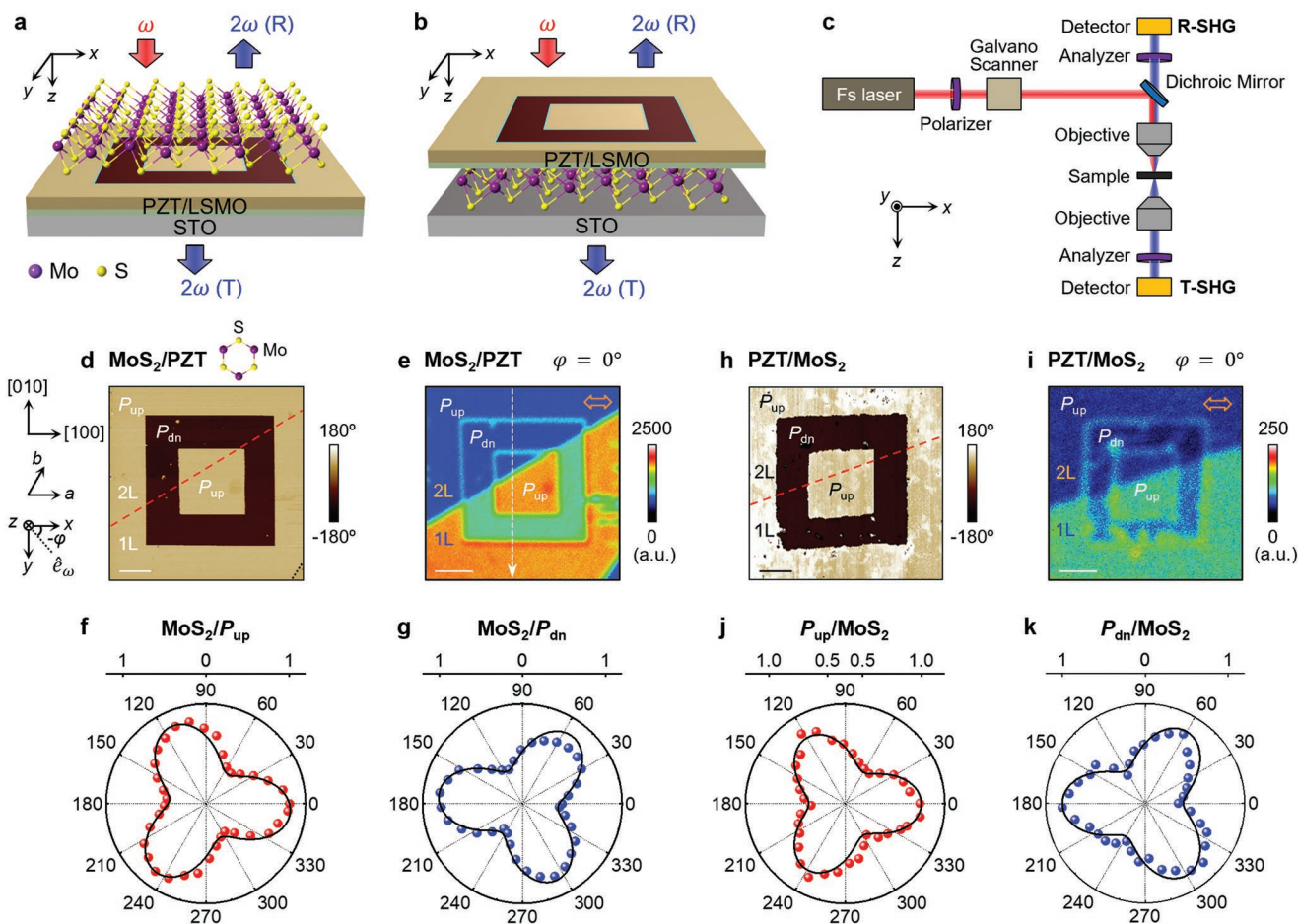


Figure 1. Ferroelectric domain control of SHG signals. a,b) Schematics of a) MoS_2/PZT and b) PZT/MoS_2 samples. c) Schematic of experimental setup. d) PFM phase image and e) T-SHG mapping of MoS_2/PZT . Inset: The laboratory coordinate system and the crystalline orientations of PZT and MoS_2 . The dashed and dotted lines in (d) mark the 1L/2L boundary and the edge of MoS_2 , respectively. The excitation laser power is 30 mW. Scale bars: 3 μm . f,g) Polar plots of normalized T-SHG intensity versus φ taken on f) P_{up} and g) P_{dn} domains in (e) with fits (solid lines). h) PFM phase image and i) R-SHG mapping of PZT/MoS_2 . The dashed line in (h) marks the 1L/2L boundary of MoS_2 . The excitation laser power is 7 mW. Scale bars: 2 μm . j,k) Polar plots of normalized R-SHG intensity versus φ taken on j) P_{up} and k) P_{dn} domains in (i) with fits (solid lines). The open arrows in (e) and (i) show the incident light polarization direction.

angle φ with respect to a -axis of MoS₂ while keeping the sample orientation fixed.

Figure 1d shows the PFM phase image of a MoS₂/PZT sample containing both 1L and 2L MoS₂ on top of prepatterned domains in PZT. We first characterize the T-SHG response with excitation laser power of 30 mW. The incident light polarization is along the horizontal DW ($\varphi = 0^\circ$) and there is no analyzer applied (Figure 1e). The 2L MoS₂ region does not exhibit noticeable SHG signal at this wavelength due to the restoration of inversion symmetry.^[2,39] In the 1L MoS₂ region, the SHG signal through the P_{up} domain is more than twice of that through P_{dn} domain (Figure 1e). Time-dependent measurements show that the tuning patterns remain stable for over 7 days, demonstrating the non-volatility of the effect (Figure S5, Supporting Information). The relative strength of the SHG intensity at the P_{up} and P_{dn} domains reverses at $\varphi = 60^\circ$ (Figure S6a,b, Supporting Information). The polar plots of the T-SHG response through the P_{up} (Figure 1f) and P_{dn} (Figure 1g) domains show threefold petal patterns, which are rotated by 60° with respect to each other. For both polar domains, the T-SHG intensity reaches extrema when the incident light polarization direction \hat{e}_ω is close to the zig-zag orientation of MoS₂ and exhibits a medium value when \hat{e}_ω is along one of the polar axes of MoS₂ \hat{P}_{MoS_2} (armchair direction) (Figure S6c, Supporting Information). This is in sharp contrast to the polarized SHG obtained on standalone MoS₂, where the SHG signal exhibits sixfold symmetry and peaks along the armchair directions. As a control study, we have also investigated the T-SHG response of MoS₂ prepared directly on STO, which exhibits an isotropic distribution independent of \hat{e}_ω (Figure S6d, Supporting Information). This result clearly shows that the angular dependence of SHG response is not affected by the nonpolar oxide layers (i.e., STO and LSMO), confirming the modification of the D_{3h} symmetry of 1L MoS₂ by the ferroelectric polarization.

For the T-SHG signal in MoS₂/PZT, the SHG response is collected through the oxide layers, where the tuning effect of ferroelectric polarization ensues. When we reverse the stacking sequence of PZT and MoS₂ (Figure 1b), similar tuning effect can be achieved by collecting the SHG signal in the reflection mode. Figure 1h,i shows the PFM phase image and R-SHG mapping, respectively, of square domains written on a PZT membrane transferred on a MoS₂ flake containing both 1L and 2L regions. To protect the PZT membrane from damage due to over-heating, we have reduced the excitation laser power to 7 mW. Despite the reduced signal-to-noise ratio, the 1L MoS₂ region exhibits clear SHG contrast between the P_{up} and P_{dn} domains (Figure 1i). The polar plots of R-SHG are qualitatively similar to those observed in the T-SHG for 1L MoS₂/PZT (Figure 1f,g): the signal exhibits threefold petal patterns peaking along the zig-zag directions of MoS₂; the patterns on the P_{up} (Figure 1j) and P_{dn} (Figure 1k) domains are rotated by 60° with respect to each other. This result clearly demonstrates the modulation of the SHG via PZT polar domains.

We consider two possible mechanisms that can account for the PZT domain-induced SHG modulation. The first is the direct coupling of the SHG signal generated by PZT and MoS₂. The SHG response of PZT, however, cannot be captured in the normal incidence/detection geometry, as its polarization is parallel to the light propagation direction or \hat{z} direction in laboratory coordinates ($\vec{P}_{\text{PZT}} \perp \hat{e}_\omega$) and does not break inversion sym-

metry in the x - y plane. This is supported by the lack of SHG response on the polar domains in bare PZT.^[38] In the second mechanism, the SHG signal of MoS₂ has been modulated directly by the polarization \vec{P}_{PZT} of PZT due to the interfacial polar coupling.^[40] To test this scenario, we apply an analyzer to evaluate the polarization of the SHG signal on the P_{up} and P_{dn} domains. We focus on the T-SHG of 1L MoS₂/PZT system for the optimal signal-to-noise ratio. Figure 2a,b shows the polar plots of T-SHG detected in the perpendicular configuration (SHG polarization direction $\hat{e}_{2\omega} \perp \hat{e}_\omega$). For 1L MoS₂ on nonpolar substrates, the SHG intensity in x - y plane exhibits sixfold symmetry (D_6) expressed as $I_\perp = I_0 \cos^2(3\varphi)$.^[1] For MoS₂/PZT, the symmetry is reduced to threefold (D_3). On the P_{up} domain, the signal peaking at $\varphi = 60^\circ, 180^\circ$, and 300° are only $\approx 70\%$ of those at $\varphi = 0^\circ, 120^\circ$, and 240° (Figure 2a). The signal on the P_{dn} domain exhibits an inverted tuning pattern (Figure 2b).

We adopt a phenomenological model to describe the polar distribution of the SHG signal. We assume that the polar coupling between MoS₂ and PZT polar domain introduces a z -component in the SHG response, with the electric field $\vec{E}(2\omega)$ expressed as $\vec{E}(2\omega) = [E_x(2\omega), E_y(2\omega), \pm A]$, where the sign of A is determined by the direction of \vec{P}_{PZT} . We hypothesize that the polarization tuning effect solely occurs at the interface and thus do not consider the phase of the SHG signal,^[41] which is supported by the fact that the SHG pattern is robust against the variation of PZT film thickness and imaging focal plane.^[38] The intensity of polarized SHG signal is given by:^[1]

$$I_{\text{SHG}} = |\mathbf{P}^{2\omega}|^2 \propto \left| \hat{e}_{2\omega} \left(d_{\text{MoS}_2}^{(2)} + d_{\text{PZT}}^{(2)} \right) \hat{e}_\omega \right|^2 \quad (1)$$

where $\mathbf{P}^{2\omega}$ is the polarization vector of the SHG light, $\hat{e}_\omega = [\cos(\varphi), -\sin(\varphi), 0]$, $d_{\text{MoS}_2}^{(2)}$ and $d_{\text{PZT}}^{(2)}$ are the second-order d -tensors for 1L MoS₂ and PZT polar domain, respectively, and $\hat{e}_{2\omega}$ is given by Equations S3 and S4 (Supporting Information). The modeled SHG intensity results for the perpendicular and parallel SHG, $I_{\perp,\parallel}(P_{\text{up,dn}})$ (Equations S5 and S6, Supporting Information), show excellent agreement with the experimental data (Figure 2a,b,d,e). The patterns on the P_{up} and P_{dn} domains fully compensate each other, with the sum $I_{\perp,\parallel}(P_{\text{up}}) + I_{\perp,\parallel}(P_{\text{dn}})$ (Equations S7 and S8, Supporting Information) recovering the sixfold symmetry of standalone 1L MoS₂ (Figure 2c,f). Assuming the perpendicular and parallel contributions have the same maximum intensity, we can reproduce the SHG signal with no analyzer by summing up $I_\perp(P_{\text{up,dn}})$ and $I_\parallel(P_{\text{up,dn}})$ (Equations S5 and S6, Supporting Information):

$$I_{\text{SHG}}(P_{\text{up,dn}}) = D \left[d_{\text{MoS}_2}^2 + 2d_{15}^2 B^2 \pm 2Bd_{15}d_{\text{MoS}_2} (\cos(3\varphi) - \sin(3\varphi)) \right] \quad (2)$$

where both B and D are fitting parameters. Equation 2 can well capture the main features observed in T-SHG for 1L MoS₂/PZT (Figure 1f,g) and R-SHG for PZT/1L MoS₂ structures (Figure 1j,k).

For the MoS₂/PZT structure, the SHG signal collected in the reflected mode does not pass through PZT, which precludes the direct tuning of ferroelectric polarization. Figure 3b shows the R-SHG mapping of the MoS₂/PZT sample shown in Figure 1e with no analyzer applied. Compared with the bare PZT domain (Figure 3a), strong SHG response is observed on the 1L MoS₂

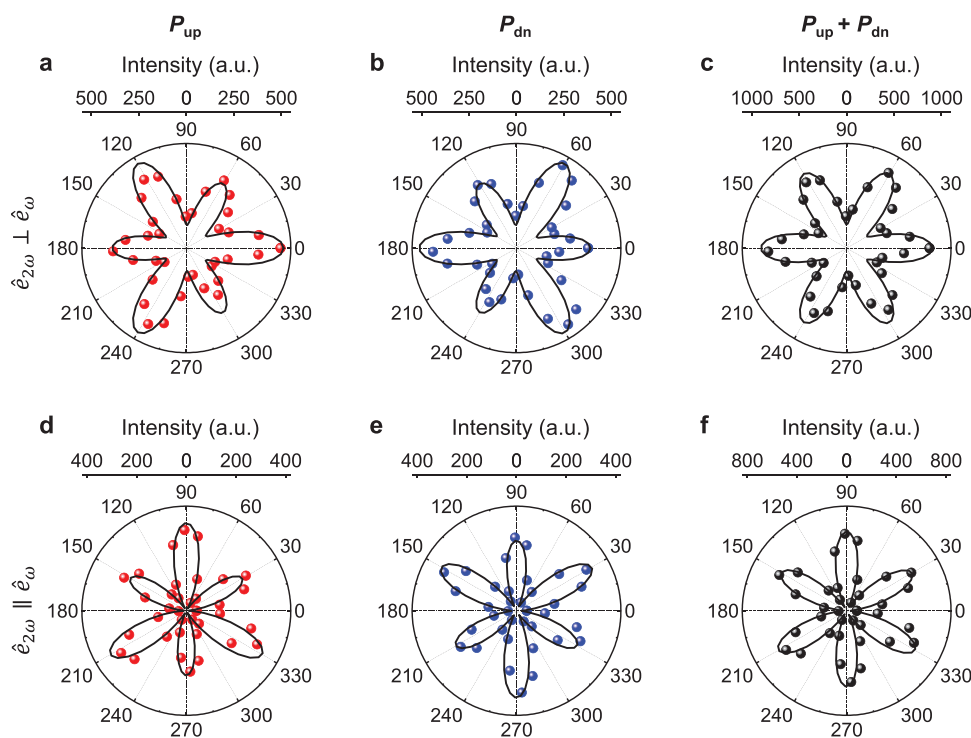


Figure 2. Polar plots of T-SHG intensity versus φ for 1L MoS₂/PZT with fits (solid lines). a–c) T-SHG in perpendicular configuration taken on a) P_{up} and b) P_{dn} domains, with c) the corresponding sum. d–f) T-SHG in parallel configuration taken on d) P_{up} and e) P_{dn} domains, with f) the corresponding sum.

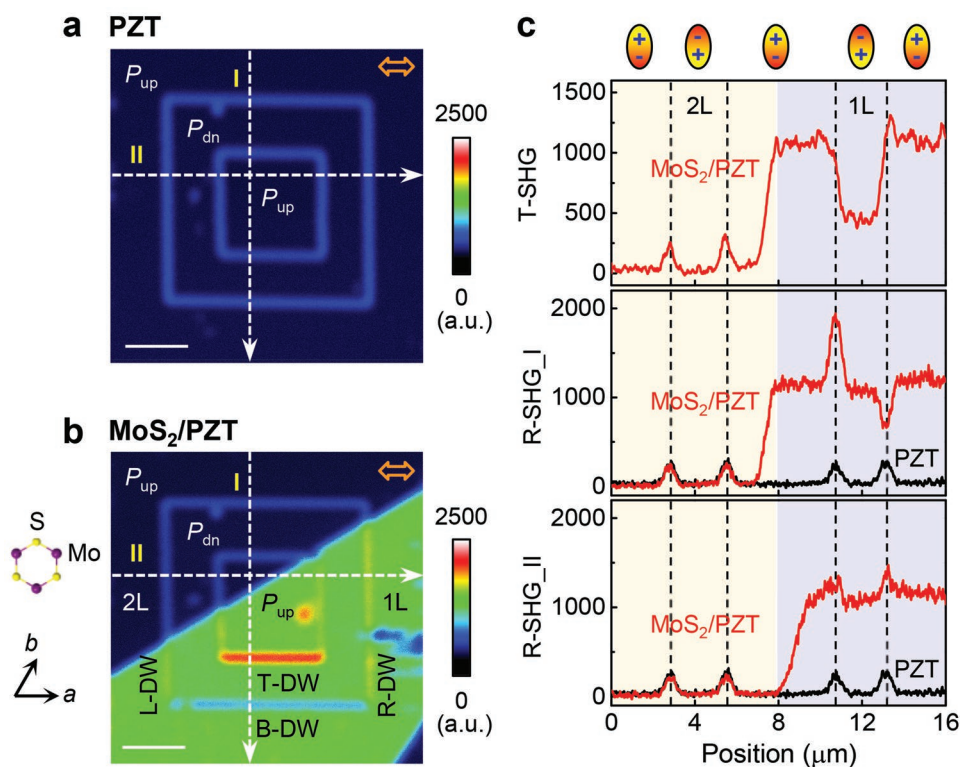


Figure 3. SHG on 1L/2L MoS₂/PZT and bare PZT. a,b) R-SHG mapping of a) bare PZT and b) the MoS₂/PZT sample in Figure 1e. The open arrows show the incident light polarization direction. Scale bars: 3 μm . c) SHG intensity profiles taken on the same MoS₂/PZT sample with the background signal subtracted. T-SHG intensity for MoS₂/PZT along the dashed arrow in Figure 1e (top panel); R-SHG intensity for MoS₂/PZT and bare PZT along the vertical arrows (middle panel) and horizontal arrows (bottom panel) in (a,b). The dashed lines indicate the DW positions.

region, while the signal intensity on the P_{up} and P_{dn} domains does not show appreciable difference.^[38] In contrast, alternating enhancement and suppression of the SHG signal emerge at the two horizontal DWs, labeled as T-DW and B-DW, which can be attributed to the alignment of the DW polarization with the polar axis of 1L MoS₂. Our previous study has shown that the in-plane polarization due to the chiral rotation of the surface dipoles at PZT DW (\vec{P}_{DW}) is comparable in magnitude with the polarization of 1L MoS₂ (\vec{P}_{MoS_2}).^[38] The enhanced (suppressed) R-SHG signal thus corresponds to the alignment (antialignment) between \vec{P}_{DW} and \vec{P}_{MoS_2} (Figure S7, Supporting Information). Such tuning effect is absent at the vertical DWs (labeled as R-DW and L-DW), where \vec{P}_{DW} is perpendicular to \vec{P}_{MoS_2} . The DW SHG signal at the 2L MoS₂ region is consistent with that of bare PZT, as expected. The distinct roles of the PZT polar domain and DW in tuning the T-SHG and R-SHG signals are clearly illustrated in the cross-sectional profiles of the SHG intensity (Figure 3c).

Next, we exploit ferroelectric DWs as an effective tool to design the SHG responses at the nanoscale. In Figure 4a, we create a hexagonal domain on PZT that conforms to the symmetry of MoS₂, with the six DWs (labeled as D1-6) making angles $\theta = 0^\circ, 60^\circ, 120^\circ, 180^\circ, 240^\circ,$ and 300° with respect to x -axis. For bare PZT without an analyzer, all DWs exhibit uniform R-SHG signals (Figure 4b). Figure 4c shows the R-SHG image taken after a 1L MoS₂ transferred on top of the hexagonal domain (a -axis aligned with D1) with the incident light polarization direction \hat{e}_ω along x -axis and no analyzer applied. The R-SHG signal is symmetric with respect to y -axis, reaching the maximum intensity at D1 ($\theta = 0^\circ$) and minimum intensity at D4 ($\theta = 180^\circ$), with $I_{SHG}(D2) \approx I_{SHG}(D6)$ and $I_{SHG}(D3) \approx I_{SHG}(D5)$.

Without the need of an analyzer, the SHG light polarization can be tuned by the DW orientation. Figure 4d–i shows the R-SHG intensity versus incident light polarization angle φ at the six DWs, which exhibit the following features:

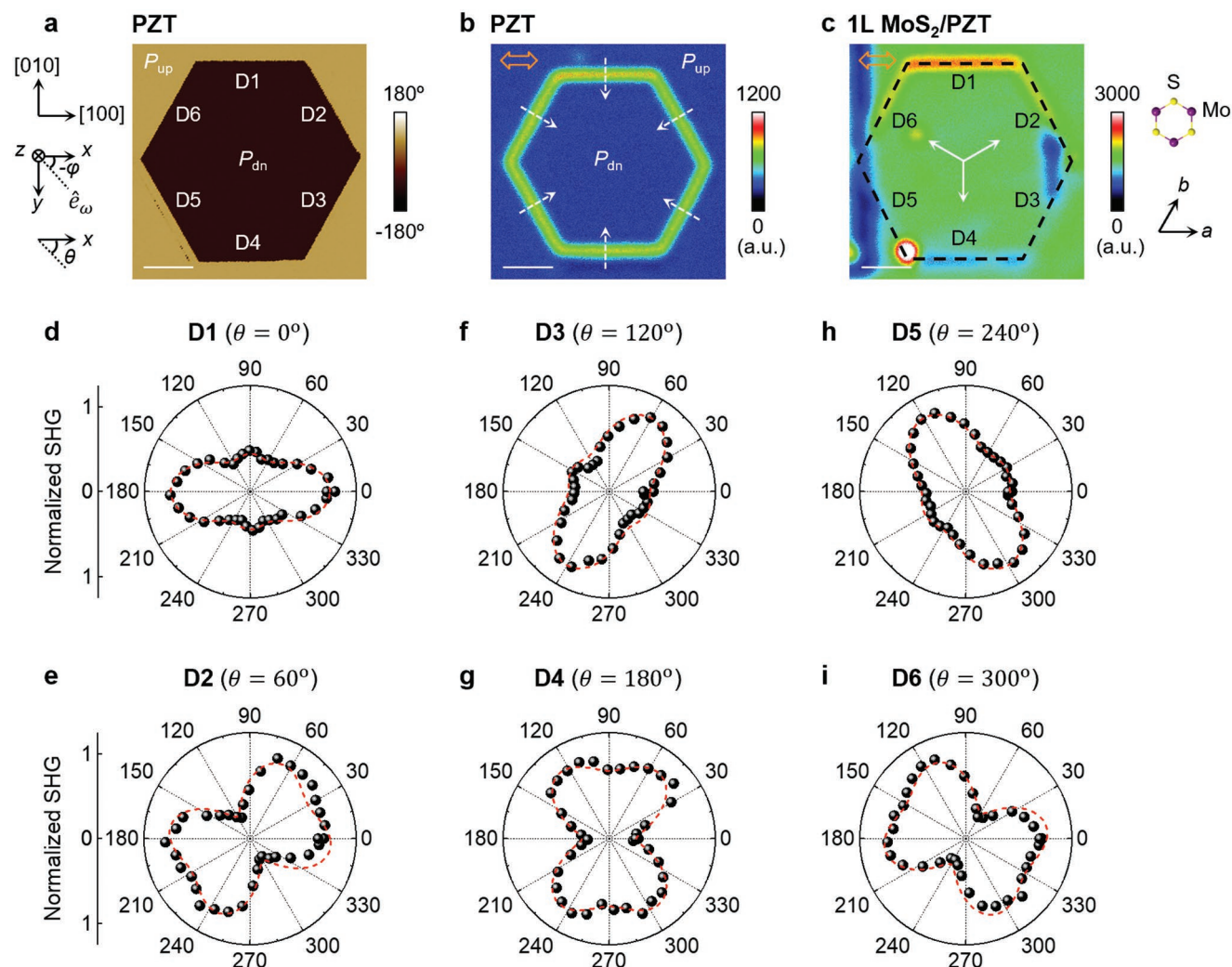


Figure 4. R-SHG tuning on 1L MoS₂/PZT DW for a hexagonal domain. a) PFM phase image and b) R-SHG mapping of a hexagonal domain on bare PZT, and c) R-SHG mapping after a 1L MoS₂ transferred on top. The open arrows show the incident light polarization direction. The dashed (solid) arrows mark the polarization directions of the DWs (MoS₂). Scale bars: 2 μ m. d–i) Polar plots of normalized R-SHG intensity versus φ taken at different DWs in (c) with fits (dashed lines).

- At all DWs, the SHG signal exhibits C_{2v} -symmetry.
- At D1 ($\theta = 0^\circ$), R-SHG reaches the maximum intensity at $\varphi = 0^\circ$ and 180° and local maxima at $\varphi = 90^\circ$ and 270° (Figure 4d). The signals at D3 ($\theta = 120^\circ$, Figure 4f) and D5 ($\theta = 240^\circ$, Figure 4h) exhibit similar angular dependence, with the pattern rotated clockwise by 120° and 240° , respectively.
- At D2 ($\theta = 60^\circ$), R-SHG reaches the maximum intensity at $\varphi = 0^\circ, 60^\circ, 180^\circ$ and 240° and minima at $\varphi = 120^\circ$ and 300° (Figure 4e). The signals at D4 ($\theta = 180^\circ$, Figure 4g) and D6 ($\theta = 300^\circ$, Figure 4i) exhibit similar angular dependence, with the pattern rotated clockwise by 120° and 240° , respectively.

Such evolution of angular-dependent SHG can be correlated to the polar alignment between \vec{P}_{MoS_2} and \vec{P}_{DW} . Monolayer MoS₂ belongs to the D_{3h} point group, with the three polar axes along the armchair directions ($\theta = 90^\circ, \theta = 210^\circ, \theta = 330^\circ$ in Figure 4c). For DWs D1, D3, and D5, \vec{P}_{DW} is parallel to one of the polar axes, while \vec{P}_{DW} of DWs D2, D4, and D6 is anti-parallel to one of the polar axes of MoS₂. The polarization of SHG at the heterointerface $\mathbf{P}_{\text{interface}}^{2\omega}$ can be obtained by summing up the second-order polarization vectors for MoS₂ $\mathbf{P}_{\text{MoS}_2}^{2\omega}$ and PZT DW $\mathbf{P}_{\text{DW}}^{2\omega}$.^[16]

$$\mathbf{P}_{\text{interface}}^{2\omega} = \mathbf{P}_{\text{MoS}_2}^{2\omega} + \mathbf{P}_{\text{DW}}^{2\omega} \propto (d_{\text{MoS}_2}^{(2)} + d_{\text{DW}}^{(2)}) \vec{E}^2(\omega) \quad (3)$$

where $d_{\text{DW}}^{(2)}$ is the second-order d -tensor for PZT DW (Supporting Information). By deriving the d -tensors of the DWs via the rotation matrix transformation, we obtain the expressions of interfacial SHG intensity at the odd- and even-numbered DWs:

$$I_{\text{D1,3,5}} = I_0 \left[C^2 \sin^2(2(\varphi - \theta_i/2)) + (C \sin^2(\varphi - \theta_i/2) - \cos^2(\varphi - \theta_i/2))^2 \right] \quad (4)$$

$$I_{\text{D2,4,6}} = I_0 \left[\sin^2(2(\varphi - \theta_i/2)) + (C' \sin^2(\varphi - \theta_i/2) + \cos^2(\varphi - \theta_i/2))^2 \right] \quad (5)$$

where $C = \frac{d_{15} - d_{\text{MoS}_2}}{d_{33} + d_{\text{MoS}_2}}$, $C' = \frac{d_{33} - d_{\text{MoS}_2}}{d_{15} + d_{\text{MoS}_2}}$, with d_{15} and d_{33} the tensor elements for PZT and d_{MoS_2} the tensor element for MoS₂, and θ_i is the orientation of the i th DW (Supporting Information). The dashed lines in Figure 4d–i show the modeled SHG results using Equations 4 and 5 with $C = 0.45$ and $C' = 0$, which are in excellent agreement with the experimental data.

For domain structures that are incommensurate with the crystal symmetry of MoS₂, the SHG polarization reflects the convoluted effect of the PZT DW and MoS₂ symmetry. Figure 5a compares the R-SHG images for a 1L MoS₂/PZT heterostructure with square domains (a -axis aligned with horizontal DWs) taken with different incident light polarization angle φ and no analyzer applied. Figure 5b–e shows the polar plots of R-SHG intensity at the four DWs [T-DW ($\theta = 0^\circ$), R-DW ($\theta = 90^\circ$), B-DW ($\theta = 180^\circ$), L-DW ($\theta = 270^\circ$)]. The angular dependence can be well fitted by Equations S9–S12 (Supporting Information), confirming the validity of the model. The distinct tuning patterns imposed by different domain structures in the absence of an analyzer clearly illustrates the power of MoS₂/PZT heterointerface in controlling the SHG polarization.

The results shown in Figures 4 and 5 have demonstrated that the MoS₂/PZT heterostructure provides effective tuning of the SHG amplitude and control of the light polarization at the nanoscale. The intensity ratio between the SHG signals at DWs with opposite \vec{P}_{DW} reaches above 4, which is comparable with those achieved via strain,^[16–18] electric field,^[7] and artificial

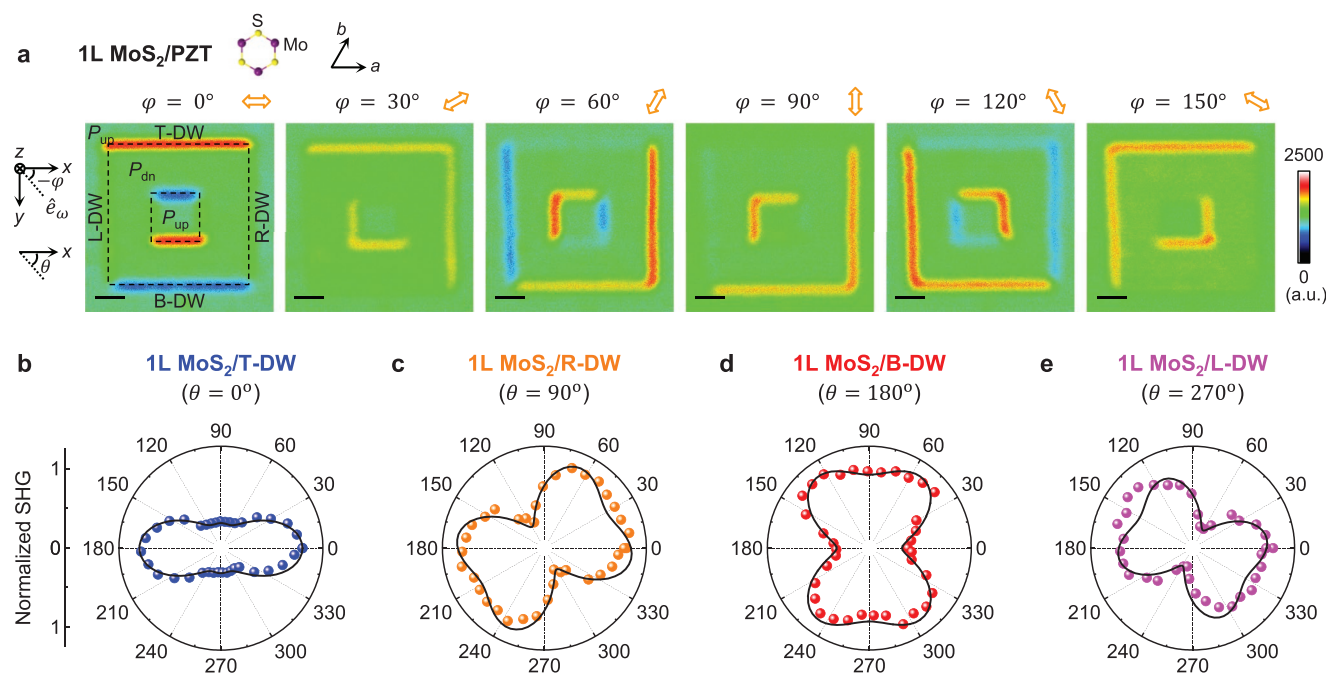


Figure 5. R-SHG tuning on 1L MoS₂/PZT DW for square domains. a) R-SHG mapping of a 1L MoS₂/PZT with square domains taken at various incident light polarization directions (open arrows) with no analyzer applied. Scale bars: 3 μm. b–e) Polar plots of normalized R-SHG intensity versus φ taken at different DWs in (a) with fits. b) 1L MoS₂/T-DW ($\theta = 0^\circ$). c) 1L MoS₂/R-DW ($\theta = 90^\circ$). d) 1L MoS₂/B-DW ($\theta = 180^\circ$). e) 1L MoS₂/L-DW ($\theta = 270^\circ$).

stacking,^[20] at room temperature. The size scaling of modulation is limited by the resolution of the SHG microscope and can be pushed down to 100 nm by working with deep-ultraviolet lasers. The MoS₂/PZT heterostructure can thus be used to construct nanoscale on-chip optical filters and optical polarizers, two important photonic components for advanced light modulators and integrated photonic circuits.^[42–44] Replacing conventional optical filter and polarizers with the MoS₂/PZT heterostructures composed of free-standing PZT membranes further enables in-operando programming of the amplitude and polarization of light, facilitating the development of smart nano-optics and integrated photonics. As the Curie temperature for epitaxial PZT films can be above 700 °C,^[45] these devices are also viable for high-temperature operations.

3. Conclusion

In summary, we report the modulation of the magnitude and polarization of SHG in monolayer MoS₂/PZT heterostructures via varying the stacking sequence and ferroelectric domain patterning. Without the need of an analyzer, the SHG signal exhibits C_{3v}-symmetry at the polar domain and C_{2v}-symmetry at the DW of PZT. The modulation is applicable over a wide range of optical excitation energy and can be realized at room temperature. Combining domain writing with free-standing PZT membranes can further lead to in-operando tuning of the nonlinear light amplitude and polarization at the nanoscale, which is nonvolatile, reconfigurable, and scalable. Our study thus presents a new material platform for developing novel optical information processing, smart optical modulators, and integrated photonic circuits.

4. Experimental Section

Preparation of PZT: Two types of (001) PZT thin film samples were prepared by using off-axis radio frequency magnetron sputtering for the SHG studies. The first type was 50 nm epitaxial PZT thin films deposited on 10 nm LSMO buffered (001) STO substrates. The LSMO layer was deposited at 650 °C in 150 mTorr process gas (Ar:O₂ = 2:1). The PZT layer was then deposited in situ at 500 °C in 120 mTorr process gas (Ar:O₂ = 2:1). The second type was free-standing PZT/LSMO membranes. 50 nm PZT/10 nm LSMO heterostructures were deposited epitaxially on 10 nm Sr₃Al₂O₆ (SAO) buffered (001) STO substrates (Figure S3a, Supporting Information). The SAO layer was deposited at 650 °C in 10 mTorr process gas (Ar:O₂ = 1:8). The PZT/LSMO/SAO/STO sample was immersed into de-ionized water to dissolve the SAO sacrificial layer. The suspended PZT/LSMO membranes were then picked up using a gel-film. The characterization details of the PZT samples can be found in the Section S2 of Supporting Information.

Raman and Photoluminescence Characterizations: The Raman and PL studies were carried out in a micro-Raman system (Renishaw InVia plus, Renishaw). Both Raman and PL spectra were collected by focusing a 514.5 nm Ar⁺ laser onto the sample surfaces at normal incidence through a 50× objective lens.

PFM Studies: The PFM studies were performed in a Bruker Multimode 8 AFM system with the conductive PtIr-coated tips (SCM-PIT, spring constant *k* of 1–5 Nm⁻¹, resonant frequency *f* of 60–100 kHz). For domain writing, a ±7 V DC bias was applied to the AFM tip. For PFM imaging, an AC voltage of 0.5 V was applied during scanning.

SHG Studies: For SHG imaging, a mode-locked Ti:Sapphire fs laser (MaiTai DeepSee HP, SpectraPhysics; wavelength: 800 nm) was used. As shown in Figure 1c, the laser beam was guided by mirrors into a

laser scanning microscope with normal incidence angle (\hat{z} direction in the laboratory coordinates) and was linearly polarized within the *x-y* plane (the sample plane). The laser beam was focused onto the sample surfaces using a water-immersed objective lens (1.05 NA, 25×). The SHG signal was collected in both transmission (T-SHG, along \hat{z} direction) and reflection (R-SHG, along $-\hat{z}$ direction) modes. The spatial resolution of SHG imaging was estimated to be about 300 nm based on the diffraction limit of the excitation laser beam (spot size: $\lambda/2NA = 380$ nm) and the second-order nonlinearity of the SHG light.

Supporting Information

Supporting Information is available from the Wiley Online Library or from the author.

Acknowledgements

This work was supported by the National Science Foundation (NSF) through grant no. DMR-2118828, DMR-1710461, and EPSCoR RII Track-1: Emergent Quantum Materials and Technologies (EQUATE), Award No. OIA-2044049. D.L. acknowledges additional support from the National Natural Science Foundation of China (grant no. 12274051) and the Fundamental Research Funds for the Central Universities (grant nos. DUT21RC(3)032, DUT21YG121). Y.L. acknowledges the support from NSF Award No. CMMI 1826392 and ONR Award No. N00014-15-C-0087. The research was performed in part in the Nebraska Nanoscale Facility: National Nanotechnology Coordinated Infrastructure and the Nebraska Center for Materials and Nanoscience, which are supported by the NSF under Award ECCS: 2025298, and the Nebraska Research Initiative.

Conflict of Interest

The authors declare no conflict of interest.

Author Contributions

X. Hong and D.L. conceived the project and designed the experiments. Q.W. and L.Z. prepared the PZT thin films. D.L. and Q.W. carried out the structural characterization of PZT. D.L. prepared the MoS₂/PZT and PZT/MoS₂ heterostructures. D.L., X. Huang, and Y.L. contributed to the Raman, PL, and SHG studies. D.L. carried out the PFM studies and performed the theoretical modeling. D.L. and X. Hong wrote the manuscript. All authors discussed the results and contributed to the manuscript preparation.

Data Availability Statement

The data that support the findings of this study are available from the corresponding author upon reasonable request.

Keywords

ferroelectric domain patterning, free-standing ferroelectric membranes, light polarization control, second harmonic generation, transition metal dichalcogenide

Received: September 25, 2022

Revised: November 8, 2022

Published online:

- [1] L. M. Malard, T. V. Alencar, A. P. M. Barboza, K. F. Mak, A. M. de Paula, *Phys. Rev. B* **2013**, *87*, 201401.
- [2] Y. Li, Y. Rao, K. F. Mak, Y. You, S. Wang, C. R. Dean, T. F. Heinz, *Nano Lett.* **2013**, *13*, 3329.
- [3] R. Wang, H.-C. Chien, J. Kumar, N. Kumar, H.-Y. Chiu, H. Zhao, *ACS Appl. Mater. Interfaces* **2014**, *6*, 314.
- [4] D. Li, W. Xiong, L. Jiang, Z. Xiao, H. Rabiee Golgir, M. Wang, X. Huang, Y. Zhou, Z. Lin, J. Song, S. Ducharme, L. Jiang, J.-F. Silvain, Y. Lu, *ACS Nano* **2016**, *10*, 3766.
- [5] A. Säynätjoki, L. Karvonen, H. Rostami, A. Autere, S. Mehravar, A. Lombardo, R. A. Norwood, T. Hasan, N. Peyghambarian, H. Lipsanen, K. Kieu, A. C. Ferrari, M. Polini, Z. Sun, *Nat. Commun.* **2017**, *8*, 893.
- [6] H. Liu, Y. Li, Y. S. You, S. Ghimire, T. F. Heinz, D. A. Reis, *Nat. Phys.* **2017**, *13*, 262.
- [7] K. L. Seyler, J. R. Schaibley, P. Gong, P. Rivera, A. M. Jones, S. Wu, J. Yan, D. G. Mandrus, W. Yao, X. Xu, *Nat. Nanotechnol.* **2015**, *10*, 407.
- [8] X.-T. Gan, C.-Y. Zhao, S.-Q. Hu, T. Wang, Y. Song, J. Li, Q.-H. Zhao, W.-Q. Jie, J.-L. Zhao, *Light: Sci. Appl.* **2018**, *7*, 17126.
- [9] N. Yoshikawa, T. Tamaya, K. Tanaka, *Science* **2017**, *356*, 736.
- [10] H. Chen, V. Corboliou, A. S. Solntsev, D.-Y. Choi, M. A. Vincenti, D. de Ceglia, C. de Angelis, Y. Lu, D. N. Neshev, *Light: Sci. Appl.* **2017**, *6*, e17060.
- [11] J. R. Schaibley, H. Yu, G. Clark, P. Rivera, J. S. Ross, K. L. Seyler, W. Yao, X. Xu, *Nat. Rev. Mater.* **2016**, *1*, 16055.
- [12] K. F. Mak, J. Shan, *Nat. Photonics* **2016**, *10*, 216.
- [13] G. Hu, X. Hong, K. Wang, J. Wu, H.-X. Xu, W. Zhao, W. Liu, S. Zhang, F. Garcia-Vidal, B. Wang, P. Lu, C.-W. Qiu, *Nat. Photonics* **2019**, *13*, 467.
- [14] K. F. Mak, J. Shan, *Nat. Nanotechnol.* **2018**, *13*, 974.
- [15] N. P. Wilson, W. Yao, J. Shan, X. Xu, *Nature* **2021**, *599*, 383.
- [16] J. Liang, J. Zhang, Z. Li, H. Hong, J. Wang, Z. Zhang, X. Zhou, R. Qiao, J. Xu, P. Gao, Z. Liu, Z. Sun, S. Meng, K. Liu, D. Yu, *Nano Lett.* **2017**, *17*, 7539.
- [17] L. Mennel, M. M. Furchi, S. Wachter, M. Paur, D. K. Polyushkin, T. Mueller, *Nat. Commun.* **2018**, *9*, 516.
- [18] S. H. Rhim, Y. S. Kim, A. J. Freeman, *Appl. Phys. Lett.* **2015**, *107*, 241908.
- [19] T. Jiang, D. Huang, J. Cheng, X. Fan, Z. Zhang, Y. Shan, Y. Yi, Y. Dai, L. Shi, K. Liu, C. Zeng, J. Zi, J. E. Sipe, Y.-R. Shen, W.-T. Liu, S. Wu, *Nat. Photonics* **2018**, *12*, 430.
- [20] W.-T. Hsu, Z.-A. Zhao, L.-J. Li, C.-H. Chen, M.-H. Chiu, P.-S. Chang, Y.-C. Chou, W.-H. Chang, *ACS Nano* **2014**, *8*, 2951.
- [21] K. Tran, G. Moody, F. Wu, X. Lu, J. Choi, K. Kim, A. Rai, D. A. Sanchez, J. Quan, A. Singh, J. Embley, A. Zepeda, M. Campbell, T. Autry, T. Taniguchi, K. Watanabe, N. Lu, S. K. Banerjee, K. L. Silverman, S. Kim, E. Tutuc, L. Yang, A. H. MacDonald, X. Li, *Nature* **2019**, *567*, 71.
- [22] L. Du, Y. Dai, Z. Sun, *Matter* **2020**, *3*, 987.
- [23] Z. Wang, Z. Dong, H. Zhu, L. Jin, M.-H. Chiu, L.-J. Li, Q.-H. Xu, G. Eda, S. A. Maier, A. T. S. Wee, C.-W. Qiu, J. K. W. Yang, *ACS Nano* **2018**, *12*, 1859.
- [24] X. Hong, G. Hu, W. Zhao, K. Wang, S. Sun, R. Zhu, J. Wu, W. Liu, K. P. Loh, A. T. S. Wee, B. Wang, A. Alù, C.-W. Qiu, P. Lu, *Research* **2020**, *2020*, 9085782.
- [25] X. Hong, *J. Phys.: Condens. Matter* **2016**, *28*, 103003.
- [26] H. Ryu, K. Xu, D. Li, X. Hong, W. Zhu, *Appl. Phys. Lett.* **2020**, *117*, 080503.
- [27] A. Lipatov, P. Sharma, A. Gruverman, A. Sinititskii, *ACS Nano* **2015**, *9*, 8089.
- [28] A. Lipatov, T. Li, N. S. Vorobeve, A. Sinititskii, A. Gruverman, *Nano Lett.* **2019**, *19*, 3194.
- [29] Z. Xiao, J. Song, D. K. Ferry, S. Ducharme, X. Hong, *Phys. Rev. Lett.* **2017**, *118*, 236801.
- [30] G. Wu, X. Wang, Y. Chen, S. Wu, B. Wu, Y. Jiang, H. Shen, T. Lin, Q. Liu, X. Wang, P. Zhou, S. Zhang, W. Hu, X. Meng, J. Chu, J. Wang, *Adv. Mater.* **2020**, *32*, 1907937.
- [31] D. Li, Z. Xiao, S. Mu, F. Wang, Y. Liu, J. Song, X. Huang, L. Jiang, J. Xiao, L. Liu, S. Ducharme, B. Cui, X. Hong, L. Jiang, J.-F. Silvain, Y. Lu, *Nano Lett.* **2018**, *18*, 2021.
- [32] R. Wang, F. Zhou, L. Lv, S. Zhou, Y. Yu, F. Zhuge, H. Li, L. Gan, T. Zhai, *CCS Chem.* **2019**, *1*, 448.
- [33] D. Li, S. Sun, Z. Xiao, J. Song, D.-F. Shao, E. Y. Tsymbal, S. Ducharme, X. Hong, *Phys. Rev. Lett.* **2021**, *127*, 136803.
- [34] W. Hou, A. Azizimanesh, A. Sewaket, T. Peña, C. Watson, M. Liu, H. Askari, S. M. Wu, *Nat. Nanotechnol.* **2019**, *14*, 668.
- [35] C. H. Li, K. M. McCreary, B. T. Jonker, *ACS Omega* **2016**, *1*, 1075.
- [36] B. Wen, Y. Zhu, D. Yudistira, A. Boes, L. Zhang, T. Yidirim, B. Liu, H. Yan, X. Sun, Y. Zhou, Y. Xue, Y. Zhang, L. Fu, A. Mitchell, H. Zhang, Y. Lu, *ACS Nano* **2019**, *13*, 5335.
- [37] P. Soubelet, J. Klein, J. Wierzbowski, R. Silvioli, F. Sigger, A. V. Stier, K. Gallo, J. J. Finley, *Nano Lett.* **2021**, *21*, 959.
- [38] D. Li, X. Huang, Z. Xiao, H. Chen, L. Zhang, Y. Hao, J. Song, D.-F. Shao, E. Y. Tsymbal, Y. Lu, X. Hong, *Nat. Commun.* **2020**, *11*, 1422.
- [39] S. Shree, D. Lagarde, L. Lombez, C. Robert, A. Balocchi, K. Watanabe, T. Taniguchi, X. Marie, I. C. Gerber, M. M. Glazov, L. E. Golub, B. Urbaszek, I. Paradisanos, *Nat. Commun.* **2021**, *12*, 6894.
- [40] J. Kaneshiro, Y. Uesu, T. Fukui, *J. Opt. Soc. Am. B* **2010**, *27*, 888.
- [41] K. J. Spychala, P. Mackwitz, M. Rüsing, A. Widhalm, G. Berth, C. Silberhorn, A. Zrenner, *J. Appl. Phys.* **2020**, *128*, 234102.
- [42] K.-H. Luo, S. Brauner, C. Eigner, P. R. Sharapova, R. Ricken, T. Meier, H. Herrmann, C. Silberhorn, *Sci. Adv.* **2019**, *5*, eaat1451.
- [43] Y. Meng, Y. Chen, L. Lu, Y. Ding, A. Cusano, J. A. Fan, Q. Hu, K. Wang, Z. Xie, Z. Liu, Y. Yang, Q. Liu, M. Gong, Q. Xiao, S. Sun, M. Zhang, X. Yuan, X. Ni, *Light: Sci. Appl.* **2021**, *10*, 235.
- [44] C. Sun, Y. Yin, Z. Chen, Y. Ye, Y. Luo, H. Ma, L. Wang, M. Wei, J. Jian, R. Tang, H. Dai, J. Wu, J. Li, D. Zhang, H. Lin, L. Li, *Photonix* **2022**, *3*, 12.
- [45] K. Wang, Y. Hao, L. Zhang, Y. Zhang, X. Chen, X. Hong, *Phys. Rev. Mater.* **2021**, *5*, 074402.